ACCRE

ACCRETE Wide-Angle Dataset

Igor Morozov, et al.
University of Wyoming

3 reports attached
additional info at:
http://w3.uwyo.edu/~seismic/accrete/

PASSCAL Data Report 02-001

Distributed by

Incorporated Research Institutions for Seismology
Data Management Center
1408 NE 45th Street
Suite 201
Seattle, Washington 98105

Generation of New Continental Crust and Terrane Accretion in Southeastern Alaska and Western British Columbia: constraints from *P*- and *S*-wave Wide-Angle Seismic Data (ACCRETE)

by Igor B. Morozov[1], Scott B. Smithson[1], Jingru Chen[1], and Lincoln S. Hollister[2]

[1]*Department of Geology and Geophysics, University of Wyoming, Laramie, WY 82071-3006*
[2]*Department of Geosciences, Princeton University, Princeton, NJ 08544*

Submitted to *Tectonophysics,* July 16, 2001
In original form: January 22, 1999; revised: July 22, 2000

Address for correspondence:

Igor B. Morozov

Department of Geology and Geophysics
University of Wyoming
PO Box 3006
Laramie, WY 82071-3006
Phone (307) 766 4905
Fax (307) 766 6679
E-mail morozov@uwyo.edu

ABSTRACT

The ACCRETE study addresses the question of continental assemblage in southeastern Alaska and western British Columbia through accretion of exotic terranes and generation of new crust by magmatic addition in a former continental arc. We present results of wide-angle *P*- and *S*-wave seismic interpretation of a 300-km long marine-land seismic line across the contacts between accreted terranes and Coast Mountains. Additional constraints on the model are obtained from correlation with geologic mapping. Our results indicate that the Coast Shear Zone (CSZ) is a nearly vertical fault zone probably related to a transpressive regime.. West of the CSZ, the mid-Cretaceous (90 Ma) thrust belt is rooted in the deep crust and is truncated by the CSZ. From the interpretation of the imaged sub-vertical reflecting zones, we infer the positions of the Alexander-Wrangellia terrane boundary and of Tertiary extensional grabens within Dixon Entrance near its intersection with the profile. The observed values of *Vp* and *Vp*/*Vs* in the lower crust of the Alexander terrane are similar to those of oceanic crust and distinctly different from the Coast Mountains Batholith (CMB) to the northeast. The crust under the CMB (32 km) is thinner than the average continental crust, and the Moho is sharp (~200 m) and highly reflective. The low-velocity mantle (7.9 km/s) suggests high temperature consistent with stability of garnet in mafic rocks in the lower crust. The lower crustal velocity of 6.9 km/s supports a lower crust composed of interlayered garnet pyroxene granulite and quartzofeldspathic-restite related to batholith generation. The crustal section under the CMB is seismically identical to the lower two thirds of normal crust, heated and inflated by intrusions of tonalite and gabbro interlayered with restites from batholith generation and uplifted during exhumation.

Key words: accreted terranes, batholith, wide-angle seismic, compressional, shear waves

INTRODUCTION

The objective of the ACCRETE project is a combined geological and geophysical study of continental assemblage by accretion of exotic terranes and generation of new crust in a continental arc. This paper presents a further analysis of the wide-angle recordings acquired during the ACCRETE transect across accreted terranes in SE Alaska and British Columbia (Fig. 1; Morozov et al., 1998). The study addresses one of the major tectonic controversies of western North America —whether terranes were accreted by essentially orthogonal (to the present day coast line) plate convergence, or whether they were emplaced during transpression from locations possibly as far south as present-day Baja California (Cowan et al, 1997). Key questions for seismic imaging are whether the features predicted by the head-on collision model, or those predicted by the translation model, can be found in the deep continental crust and the Moho. Another major target is the formation of new continental crust in the Coast Mountains batholith (CMB) in terms of thermal and deformation processes as might be manifested by the seismic velocity and reflectivity structure within the crust.

The wide-angle seismic data were obtained by marine-land recording that used the airguns and streamer of the research vessel Maurice Ewing, and REFTEK digital seismographs on land, to simultaneously obtain multichannel seismic (MCS) recordings and 3-component wide-angle seismic profiles. The acquisition of seismic data was carried out in August and September 1994. 1700 km of MCS profiling were obtained, and 28,000 airgun shots were continuously recorded by 60 REFTEK recorders on land. The airgun lines along Dixon Entrance

and Portland Canal fjord (Fig. 1) provided dense coverage of the contacts between the accreted terranes in approximately the dip direction (Fig. 1). For a further description of the experiment and for the details of the geologic and tectonic setting, see the paper by Morozov et al. (1998).

The ACCRETE seismic study is unusual in having taken advantage of marine seismic techniques in inland waterways. Along with good record quality and shot density typical for marine seismic work, such acquisition resulted in good geologic control where geologic structures could be projected down dip into the line of seismic section, probably into the lower crust. Another advantage of inland marine acquisition was the high quality and abundance of shear-wave data, apparently due to high-amplitude conversion of the airgun energy on the hard bottom of the fjord. On the negative side of inland seismic acquisition, its (expected) disadvantage was high source-induced noise level of the vertical-incidence data. Therefore, the emphasis of the seismic interpretation was put on the wide-angle recordings. Another significant complication of wide-angle data analysis was the significantly curved line of the profile (Fig. 1) combined with strong near-surface velocity variations limiting the accuracy and efficiency of traditional travel-time analysis schemes.

In this paper, we continue our recent study of the main ACCRETE corridor (Fig. 1; Morozov et al., 1998) extending our analysis to the seismic lines extending west into Dixon Entrance (Fig. 1) and enhancing the inversion using new techniques, and examining *S*-wave data. The objective of our analysis is to develop a continuous, *P*- and *S*-wave velocity structure along the entire 300-km long transect and to identify prominent crustal features across the Coast orogen. From this crustal model, we draw conclusions about the relation of the observed features

to the processes of continental growth. In another study (submitted for publication) we correlate our seismic field observations with laboratory velocity measurements and show how the environment of a former continental arc exemplified by the CMB could be a birthplace of "normal" continental crust.

DATA AND ANALYSIS

The wide-angle ACCRETE dataset consists of airgun shots at 50-100 m intervals in two passes along the fjord recorded on 3-component REFTEK seismographs deployed at 3-5-km spacing along the Portland Canal fjord (Fig. 1). From the continuous recordings at 10 ms sampling interval, we extracted 30-s travel-time-reduced shot records. Within the lines shot at 20-s intervals, this led to significant "wrap-around" between successive shots and increased data storage requirements; however, we found this redundancy useful in order to preserve the later, *S*-wave arrivals.

The ACCRETE wide-angle seismic data are generally of high quality. The most striking feature of the dataset is the abundance of very strong *S*-wave arrivals, including direct waves, Moho reflections and *P*/*S* (*S*/*P*) conversions that can often be followed to near offsets (Fig. 2). Moho *P*- and *S*-wave reflections (P_mP and S_mS, respectively) are observed in most record sections. Intracrustal *P*- and *S*-wave *S* reflections and probably *P/S* converted reflections are abundant in many records (Morozov et al., 1998)

A characteristic feature of our data processing technique is a systematic approach to data management. Data handling becomes a serious issue with the volume of the ACCRETE dataset (19 shot lines, 3-component records, about 27 GB of data in nearly 2000 files). In our data

management scheme, processing is greatly facilitated through accessing the entire data volume as a single file (Morozov, 1998). Standard data processing includes data reduction (calculation of geometric parameters, rotation of the north- and east-directed horizontal components to inline and transverse directions), filtering, and predictive deconvolution to increase resolution of crustal arrivals.

From the receiver gathers, travel times of major refracted and reflected phases were picked (Fig. 3), and the resulting picks were checked for reciprocity, although some degree of reciprocity violation was expected due to the non-surface consistent, marine-land acquisition (Morozov et al., 1998). In some cases, instantaneous 3-component amplitudes (Morozov and Smithson, 1996) were useful to highlight weaker phases and to make stable, polarization-independent amplitude measurements. The obtained travel-time curves were assembled in a database and used in subsequent analysis and inversion that included: (1) back-projection tomographic inversion of direct *P* waves, iterated with time-term inversion for sediment thickness, (2) joint, *P*- and *S*-wave forward travel-time modeling, (3) pre-stack Kirchhoff depth migration of *PmP* reflections.

Because of the crooked-line geometry (with 5 - 10% mismatches between the offsets and the in-line distances; Fig. 1) and strong non-surface consistent statics due to marine-land acquisition in a fjord, the ACCRETE data present an unusual task for conventional approaches to wide-angle analysis. Indeed, traditional crooked-line corrections would always lead to relocations of the shots (or receivers) by as much as 5 - 10 km, which is highly undesirable in the presence of strong near-surface velocity variations. One way to partly overcome this problem

was to extract statics explicitly and to use a midpoint-offset coordinate representation (Morozov et al., 1998). Here, we use a more elaborate, 2D ray-tracing scheme with full account for both 3D geometry effects and non-surface consistent statics.

Fig. 4 summarizes the main features of our travel-time modeling technique that was employed in forward modeling, tomography, and pre-stack migration. The top of the model was made very detailed based on the available bathymetry information and on the crustal basement picks performed from MCS recordings (J. Diebold, personal communication; Fig. 4) and time-term inversion of the first arrivals (Morozov et al., 1998; Chen, 1998). Since the rays approaching receivers did not travel through the sediments or water, we used a separate, simplified velocity structure under the receivers. Before modeling each receiver gather, we performed a coordinate transformation correcting for the curvature of the line. For each receiver position, this transformation consisted of stretching the 2D cross-section model so that all of the shots were placed at their correct offsets from this receiver (Fig. 4). As a result, our geometry was accurate in a 3D sense, all of the shots and receivers remained at their correct locations on the profile, and the model parameterization still remained 2D, in accordance with the general character of ray coverage. Forward ray-tracing of the selected wave types and model updating was performed interactively.

Fig. 5 shows two representative ray diagrams and the corresponding travel-times of diving waves in the crust and Moho reflections, using *P*-, *S*-, and converted waves. An abundance of *S*-wave recordings (Fig. 3) results in *S*-wave coverage equal and sometimes

exceeding that of *P* waves (Fig. 2). This abundance favors an *S*-wave travel-time analysis performed concurrently and in the same manner as the inversion of the *P*-wave data (Fig. 5).

WIDE-ANGLE SEISMIC RESULTS

Below, the results of our joint travel-time analysis of *P*- and *S*-wave, wide-angle arrivals are subdivided into three groups. First, the *P*-wave model described by Morozov et al. (1998) is refined using the modified techniques outlined above and extended to the SW, to the full, nearly 300-km length of the profile. This model is also complemented by wide-angle migration of Moho arrivals. Our second result is the *S*-wave model derived from the abundant *S*-wave and *P*/*S*-conversion travel-time data. Finally, we argue that in at least two cases, the observed *P*-wave reflections are associated with sub-vertical faults approaching the profile at oblique angles. We interpret one of these faults near the SW end of the section, in Dixon entrance as an indication of the Alexander-Wrangellia terrane boundary.

P-wave velocity structure

Fig. 6 shows the full crustal velocity cross-section from Morozov et al. (1998) with improved resolution of the uppermost crust and extended to the SW using Dixon Entrance records (Fig. 1). The average crustal velocity ranges between 6.5 and 6.6 km/s staying somewhat above the continental average (Christensen and Mooney, 1995) within the major part of the section and probably approaching this average toward the Skeena fold and thrust belt at the NE. NE of the CSZ, the Moho deepens from 23 to 32 km (Fig. 6). West of the CSZ, the new data indicate an arch in the Moho that may be related to crustal thinning due to crustal extension. Our

travel-time analysis shows that NE of Dundas Island, the Moho shallows from 25 km to approximately 23 km near the CSZ (Fig. 6). This feature cannot be attributed to the uncertainty of the unreversed ray coverage in this part of the profile.

West of Dundas Island, our model shows mid- to lower crustal velocities that are close to those under the CMB and distinctly higher than within the NE part of the model where it approaches the Skeena fold and thrust belt (Fig. 6). This difference, which is somewhat subtle in *P*-wave velocity, becomes apparent in the *S*-wave velocity structure presented below.

A group of prominent, NE dipping reflectors within the crust imaged by a number of recording stations west of the CSZ marks the mid-Cretaceous thrust system (Fig. 7). In the updated model, these reflectors are traced further SW (Fig. 6). Thus the data support the thick-skinned nature of the mid-Cretaceous thrust belt (Crawford et al., 1987) and put a better constraint on the position of its base. The termination of these reflectors in the NE and the change in the character of wide-angle reflectivity across km 40-50 of the profile suggest that the CSZ might be a near-vertical feature extending to great depth, probably close to the Moho. As we suggested earlier, such a structure could correspond to a strike-slip, crustal-scale fault associated with the Insular superterrane far-traveling between 85 and 60 Ma (Morozov et al., 1998).

Within the crust of the CMB, a number of reflectors dipping at about 20-25° NE are associated with a ductile deformation fabric observed at the surface. This fabric, east of km 90, has been identified as likely due to extension along the eastern margin of the CMB between about 50 - 52 Ma (Fig. 6; Heah, 1990; Hollister and Andronicos, 1997, 1999; Andronicos et al., 2000). As discussed in detail by Morozov et al. (1998), these and the lower-crustal reflectors

within the reversed part of the profile (0-186 km) could represent sills of gabbro within the crust or zones where velocity was increased through the formation of restites attributed to the formation of granitic plutons within the CMB (Hollister and Crawford, 1990).

P-wave Moho reflectivity

In order to examine *P*-wave Moho reflectivity along the profile and to test our ray-tracing model, we performed Kirchhoff migration of the data using our velocity model in Fig. 6. Because of the crooked-line and only approximately 2D character of our travel-time modeling, the existing migration procedures are still not adequate for accurate imaging. As a partial solution to this problem, we employed a hybrid technique (Chen, 1998), first performing the crooked-line correction and then applying a standard Kirchhoff depth migration scheme using a Seismic UNIX program by Zhenyne Liu. As has been noted by Zelt et al. (1998), our wide-angle migration is more successful in imaging the deeper part of the model. In order to reduce degradation of the image due to residual statics, imperfections in the velocity model, and pronounced 3D effects (Chen, 1998), we used trace envelopes in our migration (e.g., Simon et al., 1996).

Although the resulting image still suffers from incomplete focusing, the migration result (Fig. 8) illustrates bright and continuous coverage of the Moho with *PmP* reflections and is consistent with our travel-time model imaging the Moho upwarp SW of the CSZ and the Moho deepening NE of the CSZ. From the resulting image, the Moho west of the CSZ appears to be significantly brighter, with RMS amplitudes higher by about 50 - 60% than east of the CSZ (Fig. 9, top). Given the stability of the airgun *P*-wave source, such amplitude increase could be due to

a more reflective Moho west of the CSZ, but it also might be related to the difference in depth focusing, particularly in the case of unreversed Moho coverage west of the CSZ. In order to distinguish between these two possibilities, we examine RMS amplitudes from the raw receiver gathers presented in the bottom of Fig. 9. These records show no significant increase in the raw reflection amplitude that could account for the contrast found in the top of Fig. 9. On the contrary, the Moho *P*-wave reflectivity appears to be higher east of the CSZ, under the batholithic complex (Fig. 9, bottom). This comparison suggests that better focusing within the Moho arch (Fig. 6) is the most likely explanation of the amplitude contrast in the migrated section.

Between about km -70 to -25 of the profile, a strong dipping feature may be interpreted as sideswipe due to a shallow, near-vertical impedance contrast out of the plane of our cross-section. Further discussion of these structures will be given below.

Amplitudes of *S*-wave records and reflectivity of the Moho

The uniqueness of the ACCRETE dataset is the abundance of strong and good quality *S*-wave recordings (Fig. 2). Direct *S*-wave arrivals (*Sg*) and Moho reflections (*SmS*) can be identified in most receiver gathers, and their total amplitudes are close to or exceed the amplitudes of the *P*-wave arrivals (Fig. 3). We attribute this very unusual feature to the conditions at the bottom of the fjord which is probably rough at the scale of the *P*- and *S*-wave wavelengths at this depth (about 200 - 300 m), causing effective coupling between the *P*- and *S*-waves.

High-amplitude and consistent pre-critical *S*-wave Moho reflections indicate a sharp Moho velocity contrast along the profile (In their analysis of an N-NE extension of the profile, Hammer et al. (2000) arrived at a similar conclusion). Indeed, the dominant wavelength of *S* waves at Moho depth is about 400 m; therefore, in order to produce strong pre-critical *S*-wave reflections, the crust-mantle velocity contrast should not span significantly more than half of the wavelength, or 200 m vertically. An examination of receiver gathers near about 70 - 100 km offset (Fig. 3) shows that the Moho reflections are spatially coherent within lateral offset ranges of about 20 - 40 km. In order to estimate the lateral extents of reflective zones that are necessary to create such coherent reflections, we compare them with the inline extent of the Fresnel zone:

$$R_F \approx \frac{\sqrt{l\lambda}}{\cos\alpha},$$

where l is the total ray path length, λ is the dominant wavelength, and α is the incidence angle at the Moho. From our 2D ray-tracing at 80-km offset, $l \approx 100$ km and $\alpha \approx 55°$, and thus $R_F \approx 11$ km for *S*-waves. Although this Fresnel zone size is larger than at normal incidence, it still is significantly smaller than the observed range of lateral coherence of reflections. Therefore, it appears that the observed narrow, strongly reflecting crust-mantle transition zones span at least 10 km horizontally, and thus their aspect ratios are about 50 or greater. A possible explanation for these extended, horizontally coherent reflecting structures is their association with magmatic underplating or at the base of the crust.

Vp/Vs structure

Vp/*Vs* ratios determined from field measurements have greater potential for providing valuable constraints on crustal composition than the *P*-wave velocities alone (Christensen, 1996). This is particularly important because the *P*-wave velocity exhibits similar behavior for many common crustal rock types (e.g., Birch, 1960, 1961; Christensen and Mooney, 1995). Although it has become customary to directly associate the *Vp*/*Vs* ratios with a mechanical characteristic of the rock, the Poisson's ratio (e.g., Christensen, 1996), we will not employ this relation here in order to avoid additional ambiguity due to possible rock anisotropy and thus remain closer to the observable characteristic.

By directly comparing the *S*-wave and *P*-wave travel times for the corresponding branches, we obtain an estimate of the overall distribution of *Vp*/*Vs* within our crustal model. Fig. 10 shows *Ts*/*Tp* ratios calculated using the raw travel time picks of *Sg*, *Pg*, *SmS*, and *PmP* arrivals plotted against the corresponding midpoints. Although statics cause significant scatter in this plot and horizontal resolution is limited by offset ranges employed, the *Ts*/*Tp* ratios indicate a significant contrast in the *S*-wave velocity structure across the CSZ. West of the CSZ, a strong difference in the *Vp*/*Vs* ratios between the upper and lower crust must be present, as indicated by the difference in *Tp*/*Ts* from the direct arrivals and Moho reflections (Fig. 10). Under the CMB (km 50 - 150 in Fig. 10), the crust is more uniform in terms of the *Vp*/*Vs* ratios.

Joint inversion of *P*-, *S*-, *S*/*P* and *P*/*S* travel-time data refines the above observation and results in the *Vp*/*Vs* structure presented in Fig. 11. Since the expected resolution of the velocity ratio is lower than that of the *P*-wave velocity (e.g., Christensen, 1996), the parameterization of

the model follows that of our *P*-wave model (Fig. 6), maintaining vertically constant *Vp*/*Vs* ratios within the layers and using a minimum number of parameters horizontally.

Along with the values of *Vp* and *Vp*/*Vs*, model uncertainty is a major parameter required for an interpretation. Since our travel-time inversion technique is based on forward modeling and does not provide detailed estimates of model variance, we limited our study of model variance to the upper bound on variations of *Vp* and *Vp*/*Vs* within the lower 2/3 of the crust, which is the region most critical for our interpretation. By varying the parameters of this region, we found that about 1.5% variations in *Vp* or *Vp*/*Vs* leave the model within the residual travel-time misfits present in the final model (about 100 ms for *P*-waves and 200 – 250 ms for *S* and *P*/*S*; Fig. 5). This estimate suggests that the averaged (within a scale length of about 50 – 70 km horizontally and 10 – 15 km vertically) *Vp* values shown in Fig. 6 are accurate within about ±0.1 km/s and *Vp*/*Vs* are accurate within ±0.025 (Fig. 11).

The resulting model (Fig. 11) confirms the horizontal variation in *Vp*/*Vs* across the CSZ area and also shows somewhat higher *Vp*/*Vs* values in the middle and lower crust than the averaged values in Fig. 10. Three prominent crustal blocks are apparent in the *Vp*/*Vs* model in Fig. 11:

1) Within the crust of the Alexander terrane (west of km 20 - 40), we observe "normal" upper crust (with $Vp/Vs \approx 1.74$) while the middle and lower crust exhibit the highest *Vp*/*Vs* in our section, near 1.88. For isotropic rock, such range of velocity ratios would correspond to Poisson's ratios from 0.25 to 0.3. Note that the subhorizontal layering in this part of the model may be largely due to the unreversed ray coverage, and thus the "normal" *Vp*/*Vs* values

in the upper crust could be actually associated with the thrust belt. In such a case, the high values could be associated with the underlying crustal block.

2) Beneath the western part of the surface expression of the CMB, between the two arches in the Moho, we find a much thinner "normal" upper crustal layer of about 3 km while the middle and lower crust show *Vp*/*Vs* values between 1.78 and 1.82. Note, however, that these values are significantly lower than those normally associated with gabbros (about 1.85 - 1.86; Christensen, 1996), and correspond to Poisson's ratios between 0.27 - 0.28.

3) NE of km 120 - 130 of our profile, the entire crust shows nearly "normal" *Vp*/*Vs* of 1.74, decreasing to 1.70 within the lower crust. Although this decrease lies just outside the estimated *Vp*/*Vs* uncertainty of 0.02, two adverse factors may decrease the resolution of the velocity structure in this area: 1) the profile bends and assumes approximately strike direction near km 120, and 2) the ray coverage decreases towards the edge of the model shown in Fig. 11. Thus we consider the decrease in *Vp*/*Vs* with depth in the NE part of our section (Fig. 11) a possible feature suggested but yet not rigorously constrained by the available data.

The contrasts revealed in our model (Figs. 6 and 11) suggest significant compositional differences of the outboard Alexander terrane from the CMB. Within the Alexander terrane, we distinguish a prominent contrast between the "normal" rocks of the Mid-Cretaceous thrust belt and the high-velocity (average of 6.7 km/s), high *Vp/Vs* (1.88) underlying lower crust (Figs. 6 and 11). These values are close to the average for the oceanic crust (Christensen and Salisbury, 1982; Christensen, 1996) suggesting an association of the Alexander-Wrangellia terrane with island arcs.

Under the CMB, a moderate increase in the *Vp*/*Vs* ratio within the middle- to lower crust (Fig. 11) corroborates our earlier conclusion that the crust represents the lower two thirds of an average crustal section inflated by intrusions of high-velocity tonalite to gabbro sills (Morozov et al., 1998). These intrusions, representing the deep zone of a batholith and possibly interlayered with quartz-bearing restites, would contribute to increased values of the *Vp/Vs* ratio compared with the structure further NE and deeper into the continent (Fig. 11; Hammer et al., 2000).

Out-of-plane reflectors

In a structurally complex area, with the line of the profile gradually changing its orientation, it is possible to record out-of-plane reflections. In two cases, we identified wide-angle reflections as images of subvertical faults approaching the shot line at oblique angles (Fig. 6). Fig. 12 shows the interpretation of these features.

One of these features is a relatively weak, apparently dipping reflection crossing nearly the entire crust and surfacing near km 160 of our profile (Fig. 6). This event was identified in three wide-angle receiver gathers, and it could also be recognized in the stacked MCS section. It is discordant with any structures mapped on the surface and with other, NE dipping reflections identified in the section (Fig. 6). This feature may correspond to the fault zone (Berg et al., 1988) labeled FZ in Fig. 12.

A more prominent, and also more important for our interpretation, out-of plane reflection was found in the western part of our profile, near km -80 of the model (Fig. 6). This structure, imaged by 6 stations, produces a reflection that emerges from the first arrivals and would extend to the depth of about 15 km if it were orthogonal to the plane of our cross-section (Fig. 6). This

arrival terminates at a prominent diffraction, and, after an offset of 0.5 s, it appears to continue, probably overlapping with the *PmP* reflection (Fig. 13). Ray modeling shows that the diffraction point at the termination of this reflection corresponds approximately to the same horizontal location as the "shingling" of the *PmP* reflection (Fig. 13, near 100 km offset), and by the results of migration in Fig. 8. We interpret this combination of observations as an indication of a SE striking and probably NE dipping reflector approaching the line at an oblique angle (Fig. 12). This reflector could correspond to the boundary between the Alexander terrane and the predominantly oceanic rocks of the Wrangellia terrane. As we have shown above (Figs. 6, 11), these terranes exhibit contrasting seismic properties, and their contact could be highly reflective at wide angles of incidence.

Near about km –25 of the profile (Figs. 6), the interpreted Alexander-Wrangellia terrane boundary (AWB) is likely to have been offset by the western flank of a late Tertiary graben that is nearly orthogonal to the line of the section (Fig. 12; Rohr and Dietrich, 1992; Rohr and Currie, 1997). This is one of several grabens imaged in Dixon Entrance in the ACCRETE MCS reflection sections (Diebold, personal communication). Significant offsets in the depth of the basement are also suggested by the deepening basement in our model inferred from the first arrivals (Figs. 6 and 13). In our seismic records, the offset of the AWB is indicated by a strong diffraction (Fig. 13). Since similar diffractions occur in the same location in several record sections, they should originate from a relatively shallow velocity contrast. Thus, we conclude that the position of the AWB shown in Fig. 12 represents a shallow expression of this boundary. “Shingling” appearance of the Moho corresponding to midpoints in the same region (Fig. 13)

could also indicate that at depth, the crust of the Alexander terrane is thrust over the Wrangellia terrane.

DISCUSSION

In summary, the overall lateral variation of velocities along the profile indicates that: (1) the lower crust of the Alexander-Wrangellia terranes has higher velocity and *Vp*/*Vs,* (2) the crust of the CMB is thicker but with similar velocity ranges, although *Vp*/*Vs* decreases from the CMB to the Skeena fold and thrust belt (Figs. 6 and 11). The Alexander-Wrangellia terranes show significant contrast both between the upper and lower crust (*Vp*/*Vs* changing from 1.74 to 1.88) and with the CMB, indicating their contrasting origin and probably the presence of oceanic crust at the base of the outboard terranes. Under the CMB, the velocities change from about 6.3 km/s at 5 km depth to over 6.4 km/sec at 10 km, somewhat exceeding estimates of continental averages of 5.95 and 6.2 km/sec, respectively (Christensen and Mooney, 1995). The *Vp*/*Vs* ratios within the CMB range between 1.78 near 10 km depth and 1.82 at the base of the crust, also exceeding the continental average of 1.768 (Christensen, 1996). The relatively high velocities and *Vp*/*Vs* ratios within the CMB can be associated with the presence of tonalite and gabbro in the upper crust and gabbro, high-density restites, and layers of mafic cumulates interlayered with quartzofeldspathic rocks in the lower crust (Hollister and Crawford, 1990). However, within the eastern CMB, *Vp*/*Vs* ratios decrease vertically from 1.74 within the upper crust to 1.70 in the lower crust. Such a decrease could be related to the deeper part of our section in the NE being mostly in the Stikinia terrane, which is thought to represent the original crust prior to forming the tonalites and diorites (Gareau and Woodsworth, 1999; Hill et al., 1985).

Although the general crustal structure revealed in this study corresponds to one of the models proposed on the basis of geological observations before the seismic experiment (Crawford et al, 1987; Morozov et al., 1998), some of the findings are surprising, in particular within the CMB section. The crust under the CMB (31 - 32 km) is significantly thinner than the average continental crust (41±6 km), and lies far to the lower side of the distribution for continental arcs (39±10 km; both averages from Christensen and Mooney, 1995). At the base of the crust under the CMB velocities are 6.9 km/s. Also, the *Vp*/*Vs* ratio is moderately high at 1.82 and does not show higher values normally associated with gabbro (Poisson's ratio of 0.295, Christensen, 1996). Average crustal velocity under the CMB (6.55 km/s) is somewhat higher than the continental average (6.45±0.2 km/s; Christensen and Mooney, 1995), but this excess is mostly due to the increase in velocity in the present upper- to middle crust, between 4 - 20 km depth (Fig. 6, bottom). These observations confirm the great depth of exposure of the middle-crustal levels inferred from the estimated 15-20 km of crustal exhumation (Hollister, 1982).

The likely explanation of the lower crustal velocities lies in increased crustal and mantle temperatures indicated by wide-angle velocity measurements in this area (Morozov et al., 1998; Hammer et al., 2000). The *Pn* velocity of 7.9 km/s obtained in both of these studies is significantly lower that the continental average (8.1±0.2 km/s) and close to the average for continental arc regions (7.9±0.2 km/s; Christensen and Mooney, 1995). This low *Pn* velocity combined with high regional heat flow values of 82 mW/m² (Lewis, 1992) indicates high temperatures at the base of the crust. A sub-Moho velocity of 7.9 km/s approximately corresponds to a temperature of about 800° C, although the *Vp-T* become non-linear in this range

(Kern and Richter, 1981). Phase relations indicate that garnet would be stable in mafic lower crustal rocks at these temperatures (Ringwood, 1975) so that mafic underplating would be represented by garnet pyroxene granulites. Also, a linear correlation of increasing Poisson's ratio with decreasing SiO_2 content has been observed (Christensen, 1996). Thus the presence of quartz-bearing layers interlayered with gabbro may be another possible reason for the absence of "mafic" *Vp*/*Vs* ratios within the lower crust under the CMB. V_P and V_P/V_S relationships are consistent with a batholith origin by intrusion of mafic sills to melt metasedimentary rocks resulting in a lower crust of interlayered garnet pyroxene granulite and restite derived from a quartzofeldspathic protolith. An alternative hypothesis is that the batholithic rocks were derived from melting of amphibolite in the lower crust (Thomas and Sinha, 1999).

The higher than average crustal velocities and *Vp/Vs* ratios under the CMB, especially in the middle crust, reflect the fact that the present-day mid- and upper crust is inflated by basaltic intrusions that provided the heat for the generation of the batholith. The crust is also much thinner than normal, indicating that the great uplift since the formation of CMB 60 Ma ago (Hollister, 1992) involved the entire crust also raising *Vp* and *Vp*/*Vs* at any given depth level. A combined geological evidence for this uplift is the crustal unroofing by extension, listric faults, and mineral pressure-temperature conditions (Hollister, 1992). Taking this uplift and the increased crustal temperature into account, the crustal CMB section can thus be interpreted as the lower two thirds of “normal” continental crust. The contrast across the CSZ between the crust of the CMB and of the mid-Cretaceous thrust belt becomes apparent in the *Vp*/*Vs* domain (Fig. 11) and is most likely related to the presence of a remnant of an island arc within the lower crust of the outboard terranes.

CONCLUSIONS

The ACCRETE study represents one of the first detailed seismic images through a continental arc where new crust has been formed. Employing marine wide-angle seismic techniques in a fjord, we took advantage of dense subsurface coverage and high-quality shear-wave data combined with good geologic control to constrain seismic results. The crustal velocities and dipping reflectors in the mid-Cretaceous thrust belt and the CMB can be correlated directly with lithologies observed on the surface and projected into the seismic section. Three groups of results arise from our interpretation of the complete ACCRETE transect:

1) Crustal thickness and V_P/V_S in the **Alexander-Wrangellia terrane** are **distinctly different** from the CMB strongly suggesting its exotic origin. The lower crust of Alexander terrane has *Vp* and *Vp*/*Vs* characteristics similar to those of oceanic crust. Under Dixon Entrance, the position of the Alexander-Wrangellia terrane boundary is inferred from out-of plane wide-angle reflections. This terrane boundary is probably offset by the flanks of Tertiary grabens identified in previous studies.

2) **The Coast Shear Zone** appears as a nearly vertical feature marked by the termination of reflectivity from both SW and NE, and by crustal thickening. West of the CSZ, the mid-Cretaceous (90 Ma) thrust belt is rooted in the deep crust and is truncated by the CSZ, as predicted by Crawford et al. (1987). The truncation of this thrust belt suggests that it may have formed elsewhere and that the CSZ is a younger, strike-slip fault zone along which the thrust belt was translated to its present position. Thus this study suggests that the CSZ is probably related to a transpressive regime (Andronicos et al., 1999).

3) **The crustal section under the Coast Mountains Batholith** (CMB) represents the lower two thirds of normal crust inflated by intrusions of tonalite and gabbro. *P*-wave velocity and *Vp*/*Vs* ratio show a distinct decrease toward the Skeena fold and thrust belt. The crustal thickness within the entire interpreted section varies from 23 to 32 km. Moho is sharp (~200 m in thickness) and highly reflective, with horizontal correlation length on the order of 5-15 km. Such a sharp Moho with a particularly strong *S*-wave reflectivity might result from basaltic partial melts at the base of the crust. Low-velocity (7.9 km/s), probably hot mantle should contribute heat leading to increased temperature in the lower crust and garnet stability in mafic rocks. Lower crust can be interpreted as tonalite and gabbro intrusions, metamorphosed to garnet pyroxene granulites, and restites from batholith generation, including quartz-bearing rocks. The higher than average crustal velocities in the CMB reflect the fact that the lower velocity (more felsic, approximately granodioritic) material of the upper crust has been removed. *P*-wave and especially *S*-wave modeling shows that the CMB portion of the crustal section (Figs. 6 and 11) can be considered as corresponding to the lower two thirds of an average crustal section which has been inflated by intrusions of shallowly dipping, high-velocity tonalite to gabbro sills into the crust, with increasing proportion of gabbro sills in the lower crust.

As an overall conclusion, generation of new crust within a former continental arc results in average crustal velocities of about 6.55-6.6 km/s (at normal crustal geotherm) in the lower 3/5 of the crust. This would lead to an average crustal velocity of ~6.4 km/s with 10-15 km of the upper crust restored. This model can explain the formation of a typical continental crust.

ACKNOWLEDGMENTS

We thank the management and crew of the R/V Maurice Ewing, directed by John Diebold and the crew of the charter boat *Barbara K*, under the direction of Bill Crawford, Maria Louisa Crawford, and Chris Humphreys. Essential help in the deployment of the seismometers was provided by the Department of Geophysics and Astronomy of the University of British Columbia. We thank Marcos Alvarez of the Stanford IRIS center for his help with instrumentation and programming. The field work and ship operations were facilitated by the Canadian Coast Guard, Prince Rupert Base. We thank the people of the Prince Rupert and Ketchikan regions for their active support of the seismic experiment. Peter Carroll and the LITHOPROBE management at the University of British Columbia provided exceptional assistance with obtaining the official permits for the seismic experiment. Numerous comments and suggestions by Ron Clowes helped to improve this manuscript. Our work on this project was supported by NSF grants EAR-92-18482, EAR-92-19294, and EAR-95-26753. Processing and interpretation was carried out at the University of Wyoming Seismic Computing Laboratory.

REFERENCES

Andronicos, C. L., Hollister, L. S., Davidson, C., and Chardon, D., 1999. Kinematics and tectonic significance of transpressive structures within the Coast Plutonic Complex, British Columbia. Journal of Structural Geology, 21, 229-243.

Andronicos, C.L., Rusmore, M.E., Chardon, D.H., Hollister, L.S., and Davidson, C., 2000. Eocene crustal extension within the Coast Plutonic Complex. Geological Society of America Abstracts with Programs 32, no.6, A2.

Berg, H. C., Elliott, R. L., and R. D. Koch, 1988. Geologic map of Ketchikan and Prince Rupert quadrangles, southeastern Alaska: U.S. Geological Survey Miscellaneous Geologic Investigations Map I-1807, scale 1:250,000.

Birch, F. 1960. The velocity of compressional waves in rocks to 10 kilobars, 1, J. Geophys. Res., 65, 1083-1102.

Birch, F. 1961. The velocity of compressional waves in rocks to 10 kilobars, 2, J. Geophys. Res., 66, 2199-2224.

Chen, J. 1998. Seismic wide-angle migration across the Coast Mountains orogen in southeast Alaska and British Columbia, Masters Thesis, University of Wyoming.

Christensen, N. I., 1979. Compressional wave velocities in rocks at high temperatures and pressures, critical thermal gradients, and crustal low-velocity zones, J. Geophys. Res., 84, 6849-6857.

Christensen, N. I., 1996. Poisson's ratio and crustal seismology, J. Geophys. Res.,101, B2: 3139-3156.

Christensen, N. I., Mooney, W. D., 1995. Seismic velocity structure and composition of the continental crust: A global view, Journ. Geophys. Res.,100, B7: 9761-9788.

Christensen, N. I., Salisbury, M. H. 1982. Lateral heterogeneity in the seismic structure of the ocean crust inferred from velocity studies in the Bay of islands ophiolite, Newfoundland, Geophys. J. R. Astron. Soc., 68, 675-688.

Cowan, D. S., Brandon, M. T., Garver, J. I., 1997. Geologic tests of hypotheses for large coastwise displacements-A critique illustrated by the Baja British Columbia controversy: American Journal of Science, 297: 117-173.

Crawford, M. L., Hollister, L. S., Woodsworth, G. L., 1987. Crustal deformation and regional metamorphism across a terrane boundary, Coast Plutonic Complex, British Columbia, Tectonics, 6: 343-361.

Gareau, S.A., and Woodsworth, G.J., 1999, Yukon-Tanana terrane in the Scotia-Quaal belt, Coast Plutonic Complex, central-western British Columbia; Tectonics of the Coast Mountains, southeastern Alaska and British Columbia, H.H. Stowell and W.C. McClelland (ed.); Geological Society of America, Special Paper 343, p. 23-43.

Hammer, P., Clowes, R., Ellis, R., Crustal structure of NW British Columbia and SE Alaska from seismic wide-angle studies: Coast Plutonic Complex to Stikinia: JGR, 2000.

Heah, T. S. T., 1990. Eastern margin of the Central Gneiss Complex in the Shames River Area, Terrace, British Columbia, *in:* Current Research, Part E, Geological Survey of Canada Paper 90-1E, Geological Survey of Canada: 159-169.

Hill, M. L., Woodsworth, G. J., and van der Heyden, P., 1985, The Coast Plutonic Complex near Terrace, British Columbia: A metamorphosed western extension of Stikinia: Geological Society of America, Abstracts with Programs, v. 7 p. 362.

Hollister, L. S., 1982. Metamorphic evidence for rapid (2 mm/yr) uplift of a portion of the Central Gneiss Complex, Coast Mountains, B. C., Canadian Mineralogist, 20, 319-332.

Hollister, L. S., Andronicos, C. L., 1997. A candidate for the Baja British Columbia fault system in the Coast Plutonic Complex,. GSA Today, 7 (11), 1-7.

Hollister, L. S., Crawford, M. L., 1990. Crustal formation at depth during continental collision, *in:* Salisbury, M. H., and Fountain, D. M. (Eds.), Exposed cross-sections of the continental crust, Nywell, MA, Kluwer: 213-226.

Hollister, L.S., Das, T., Diebold, J.B., Morozov, I.B., Smithson, S.B., 1997. Evidence for late (Miocene?) extension across the Coast Mountains. LITHOPROBE Report No. 56: 215-218.

Kern, H., Richer, A., 1981. Temperature derivatives of compressional and shear seismic velocity in crustal and mantle rocks at 6 kbar confining pressure, J. Geophys., 49, 47-56.

Lewis, T., 1997. In-Slave Northern Cordillera Lithospheric Evolution (SNORCLE) Transect and Cordilleran Tectonic Workshop Meeting (March 7-9, University of Calgary, F. Cook and P.

Erdrres (compilers), Lithosheric Report No. 56, University of British Columbia, pp. 221-222.

Morozov, I. B., 1998. 3D seismic processing monitor, Computers & Geosciences, 24 (3), 285-288.

Morozov, I. B., Smithson, S. B., 1996. Instantaneous polarization attributes and directional filtering, Geophysics, 61, 872-881.

Morozov, I. B., Smithson, S. B., Hollister, L. S., Diebold, J. B., 1998. Wide-angle seismic imaging across accreted terranes, Southeastern Alaska and Western British Columbia, Tectonophysics, 299, 281-296.

Newton, R. C., Hansen, E. C., 1983. The origin of Proterozoic and late Archean charnockites; evidence from field relations and experimental petrology, Mem. Geol. Soc. Am., 161, 167-179.

Ringwood, A. E., 1975. Composition and petrology of the Earth's mantle, McGraw-Hill, New York.

Rohr, K. M. M., Currie, L., 1997. Queen Charlotte basin and Coast Mountains: Paired belts of subsidence and uplift caused by a low-angle normal fault, Geology, 25 (9), 819-822.

Rohr, K. M. M., Dietrich, J. R., 1992. Strike-slip tectonics and development of the Tertiary Queen Charlotte basin, offshore western Canada: Evidence from seismic reflection data, Basin Research, 4., 1-19.

Simon, H., Gebrande, H., Bopp, M, 1996. Pre-stack migration and true-amplitude processing of DEKORP near-normal incidence and wide-angle reflection measurements, Tectonophysics, 264, 381-392, 1996.

Thomas, J. B., Sinha, A. K., 1999. Field, geochemical, and isotopic evidence for magma mixing and assimilation and fractional crystallization processes, In: The Quottoon Igneous Complex, Northwestern British Columbia And Southeastern Alaska, Can. J. Earth Sci., 36, P. 819-831.

Zelt, B. C., Talwani, M., Zelt, C. A., 1998. Prestack depth migration of dense wide-angle seismic data, Tectonophysics, 286, 193-208.

Figures

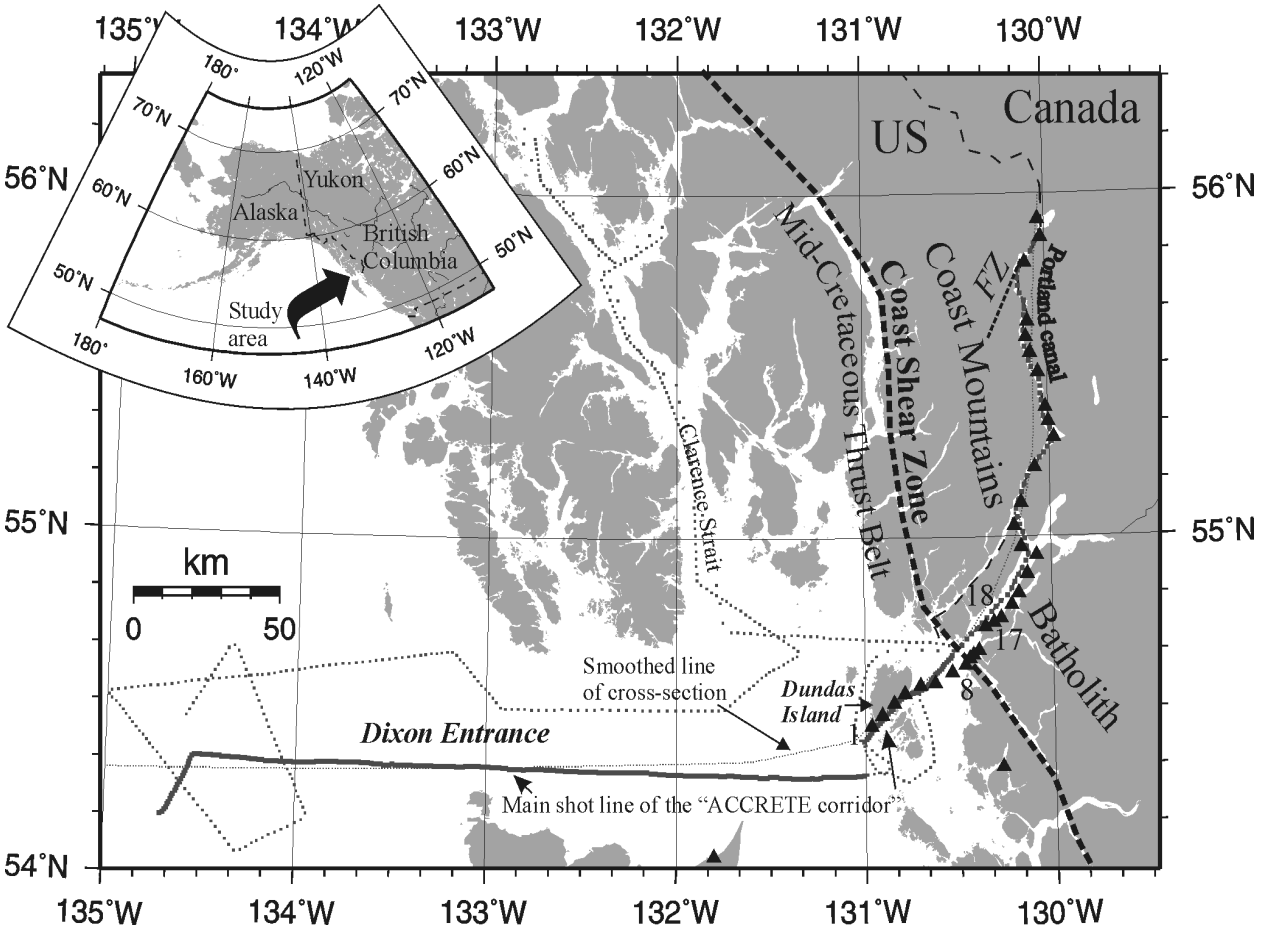

Fig. 1. Location map of the ACCRETE seismic wide-angle experiment area discussed in this paper. Triangles indicate REFTEK recording sites; main airgun shot lines are shown in heavy dotted and solid lines; additional shot lines are shown in light dotted lines. Numbers indicate the locations of recording stations used in Figs. 3, 5, 7 and 13. FZ is a subvertical fault zone (Berg et al., 1988) imaged in this study.

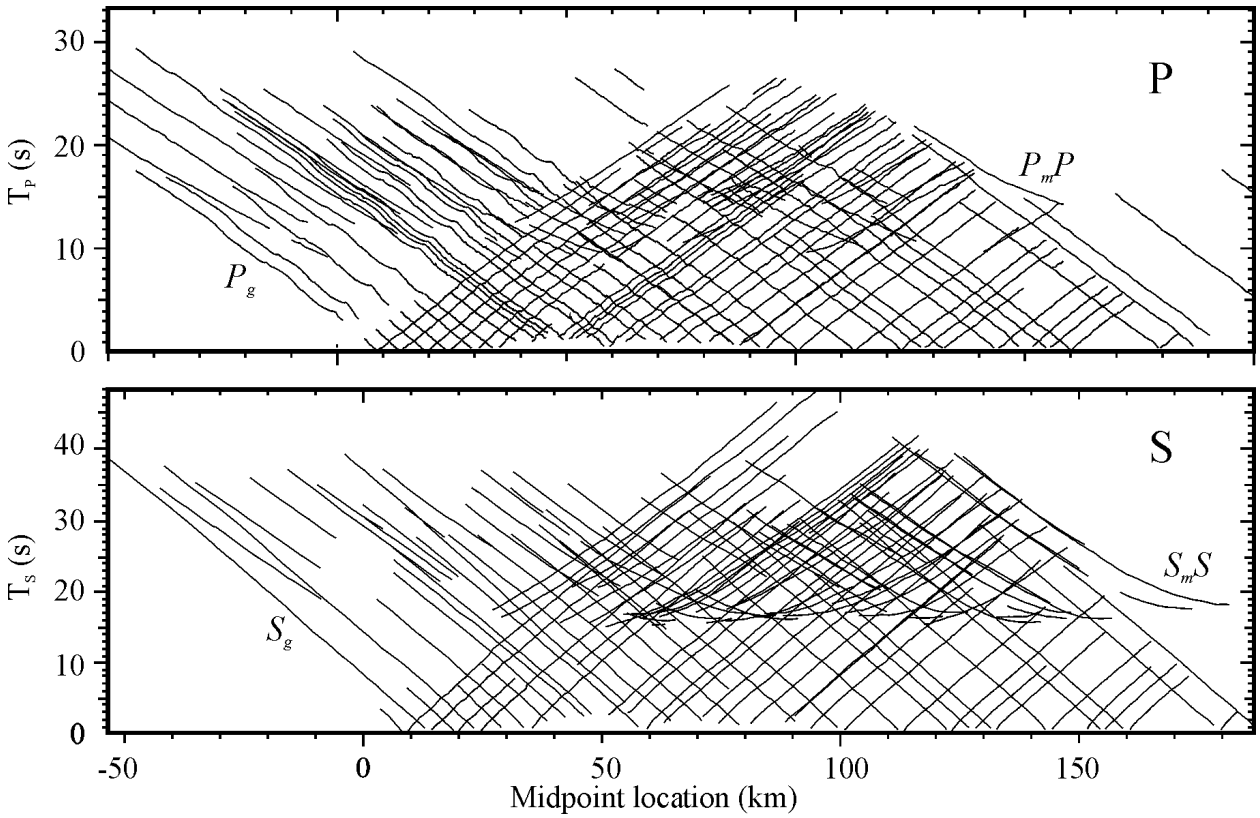

Fig. 2. Direct-wave (curves emerging from near-zero times) and Moho reflection (the rest) travel-time coverage of *P*- and *S*-waves along the ACCRETE corridor. Picked seismic phases are plotted versus their midpoints on the line of cross-section. Note the high fold and continuous sampling of both the crust and the Moho. Also note that the *S*-waves often provide longer offset ranges of Moho reflections than the *P*-waves.

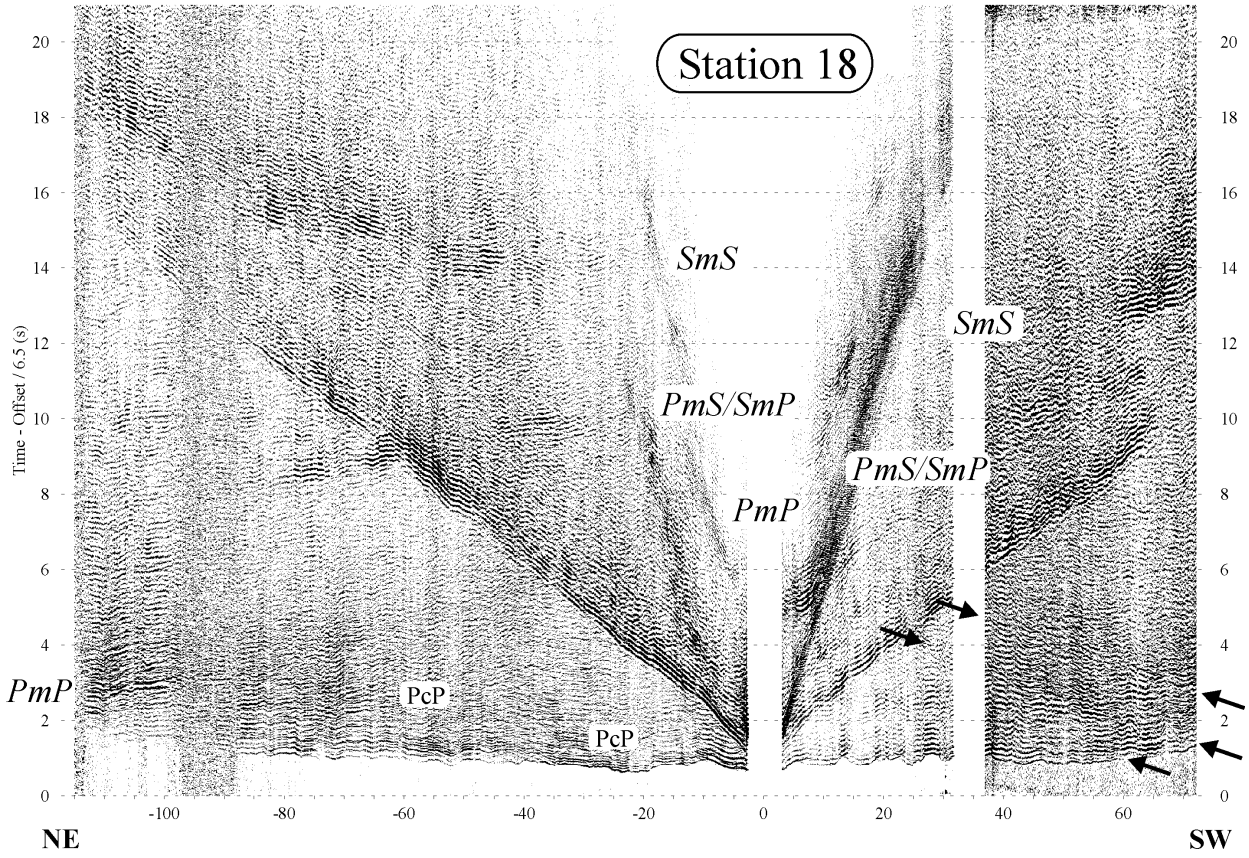

Fig. 3. Inline-component records from station 18 emphasizing the unusually good recordings of *S* waves. Reduction velocity is 6.5 km/s. Note that the Moho *P*-, *S*, and *P*/*S*-wave reflections can be traced to small pre-critical offsets (Fig. 2). We interpret the observations of pre-critical reflections as an indication of a sharp Moho. Also note the asymmetry in the *SmS* and *PmS* reflections indicating a variation of Moho depth across the CSZ. Arrows indicate reflections from the SE-verging mid-Cretaceous thrust belt SW of the CSZ (Morozov et al., 1998).

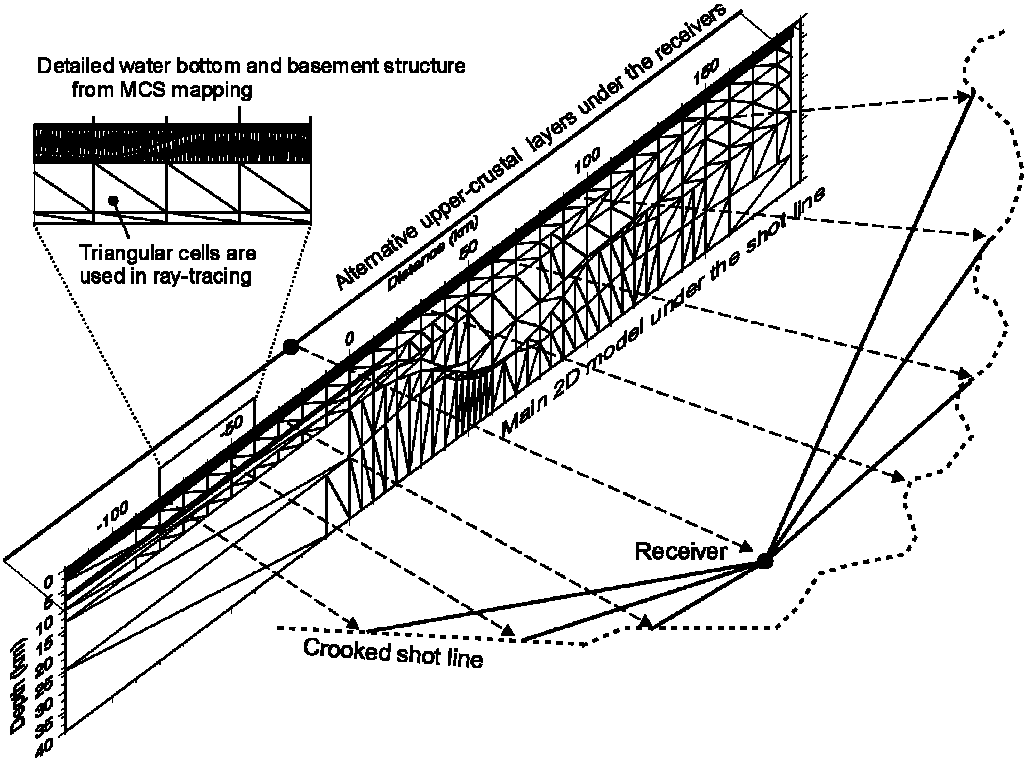

Fig. 4. Ray-tracing approach employed in this study. The 2D subsurface model is associated with a smoothed (yet strongly bending) profile of cross-section. The horizontal coordinates of the model are transformed (dashed arrows) before tracing of each receiver gather in order to ensure accurate source and receiver locations and offsets at the same time. To account for the on-land recording along the shores of the fjord, we introduce "alternative" model layers without sediment cover under the receivers. Ray tracing is based on triangulation of the model into cells with constant *P*- and *S*-wave velocity gradients. Note the detailed upper layers of the model derived from the bathymetry data and from the basement depth picks made from MCS data (John Diebold, personal communication). Model nodes contain independent *Vp* and *Vp*/*Vs* parameters updated interactively using simultaneous tracing and displays of the travel times of *P*-, *S*-, and converted waves (Fig. 5).

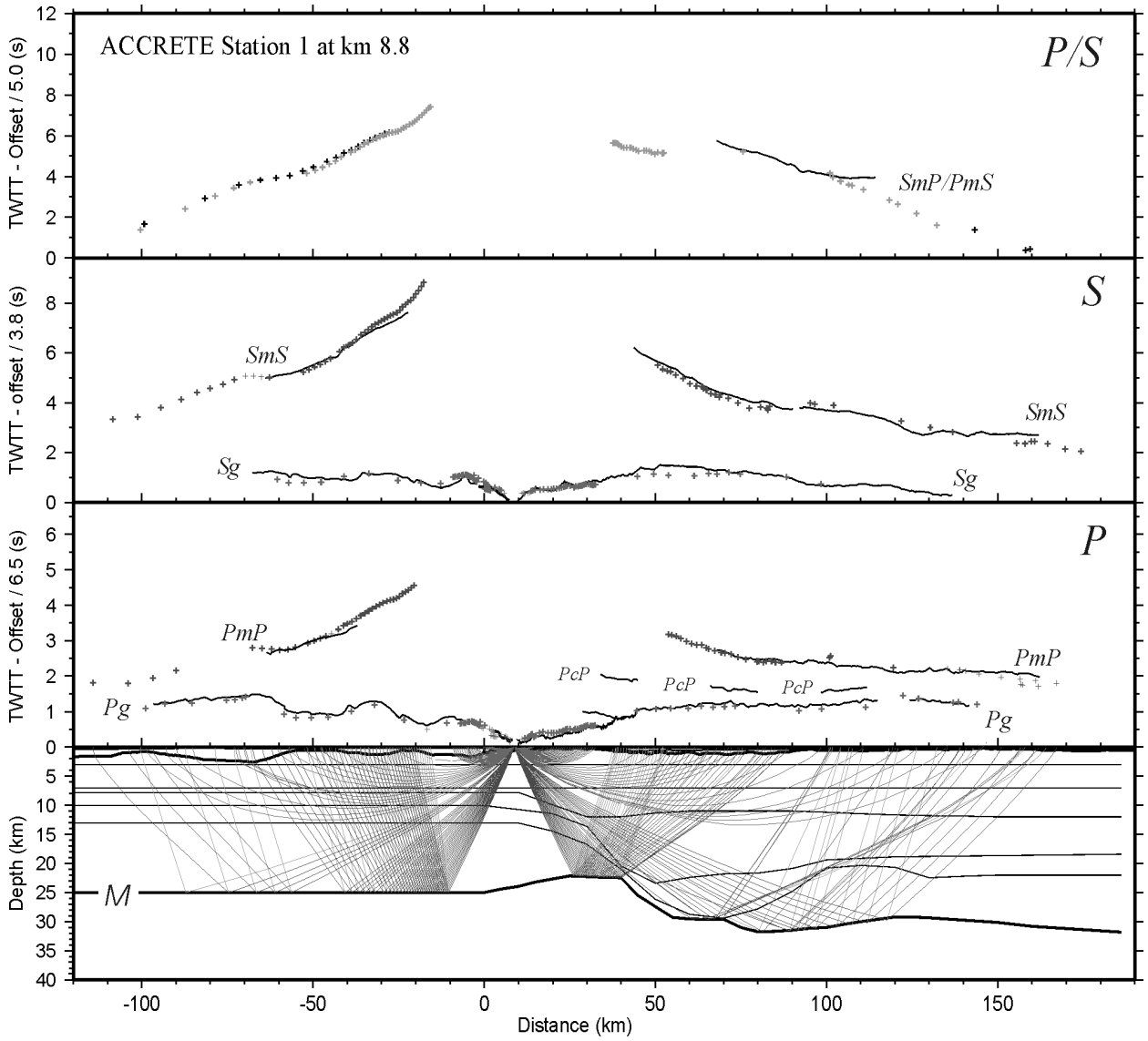

Fig. 5. Ray diagrams and the corresponding travel-time fits for two stations of the wide-angle ACCRETE corridor lines. Lines are the travel-time picks, small crosses represent the computed travel times. Only the crustal diving waves and Moho reflections and their computed travel times are shown. The event labeled FZ is interpreted as a reflection from the subvertical fault zone shown in Fig. 1.

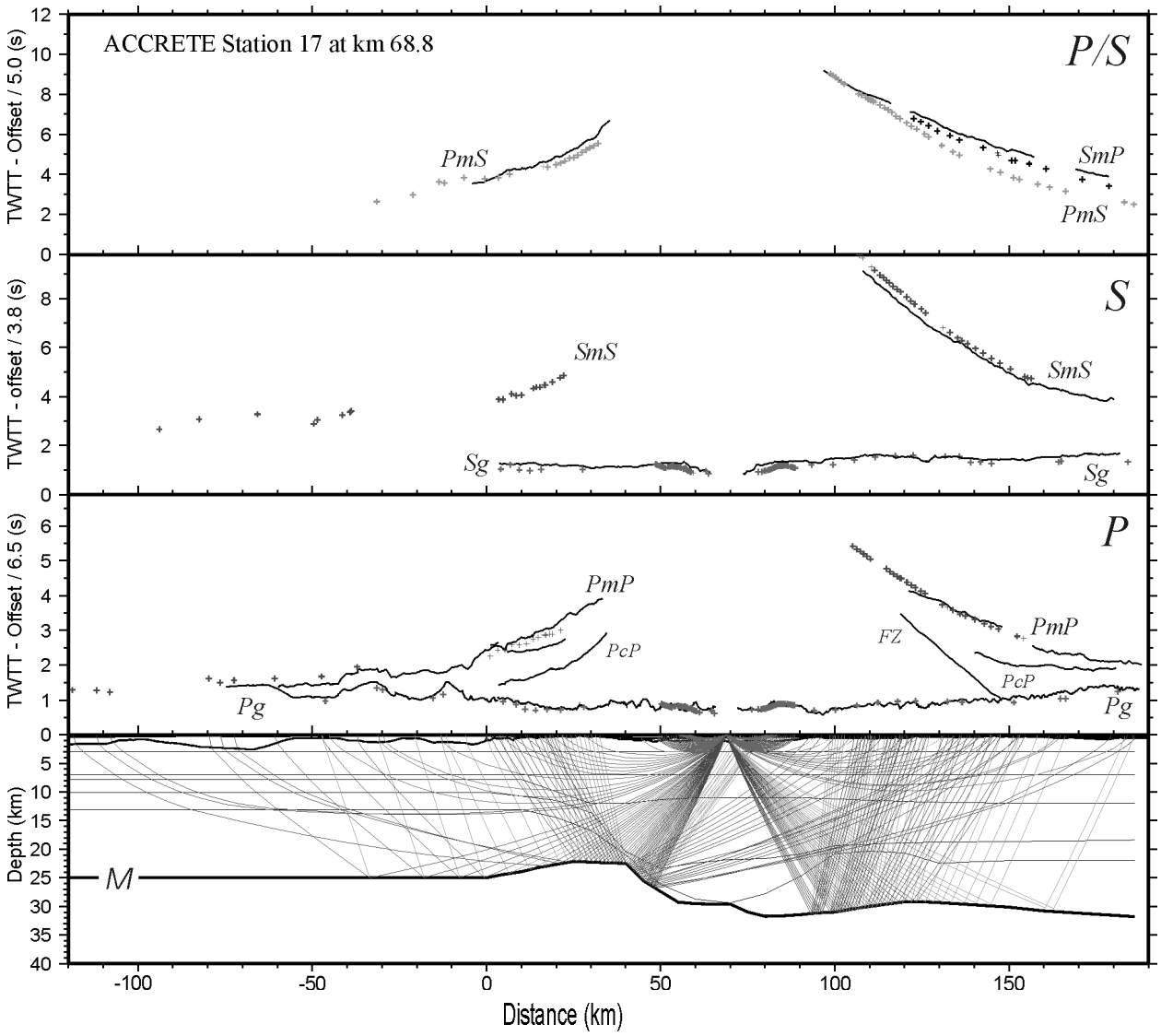

Figure 5 (continued)

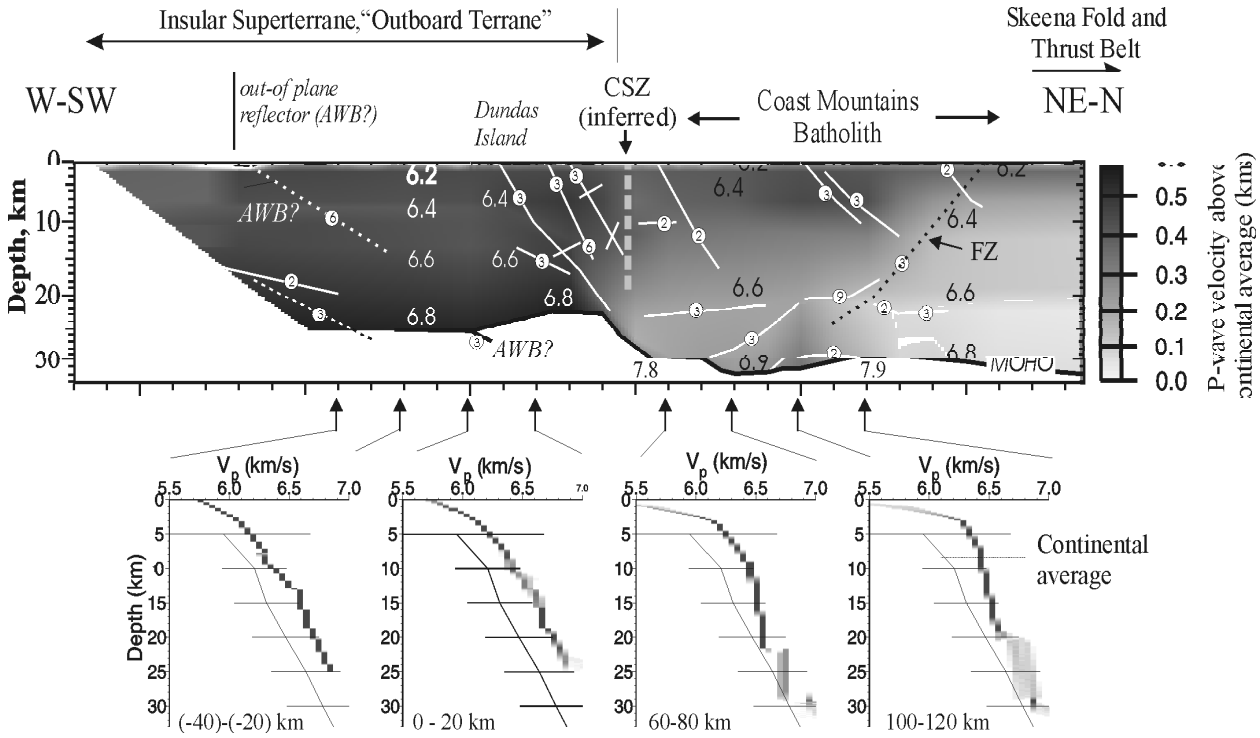

Fig. 6. *Top*: *P*-wave velocity model for the crust along the ACCRETE corridor by Morozov et al (1998; NE of km 0 here) and extended to the W-SW. Vertical exaggeration is 2:1. Velocity values are given in labels; gray shading shows velocity relative to the average continental crustal model (Christensen and Mooney, 1995). Surface locations of the Coast Shear Zone (CSZ) and of the Coast Mountains Batholith (CMB) are shown. Locations of subvertical faults are inferred from seismic data. The imaged reflecting boundaries are labeled with the number of recording stations used to constrain them (small circles). Dotted lines show out-of-plane reflectors: the late Tertiary grabens (*TG*, see also Figs. 12 and 13) and a fault zone mapped in the NE CMB (FZ, Berg et al., 1988; Fig. 1) rotated into the plane of the cross-section. Note the offset of the TG reflectors and a possible step on the Moho caused by the Clarence Strait Fault (see the text for discussion). Estimated mantle velocity values are given in labels. *Bottom*: vertical velocity profiles at selected locations in the model, also compared to the continental average (Christensen and Mooney, 1995). Shading in the bottom plots indicates horizontal velocity variation within the specified distance ranges.

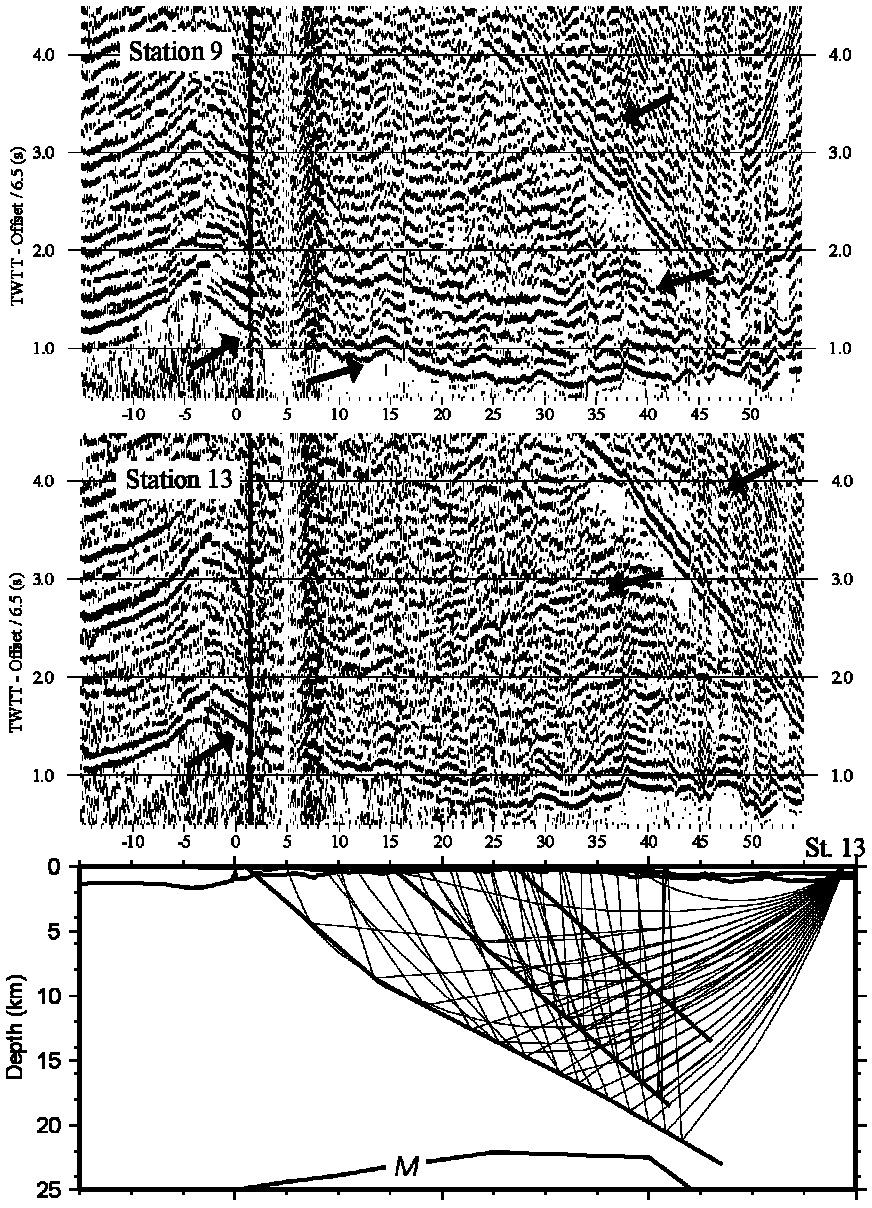

Fig. 7. NE- dipping reflectors delineating the Mid-Cretaceous thrust belt within the crust. Although these reflections are typically not strong enough to be correlated to full length from single receiver gathers, correlation of two to four of those gathers increases our confidence in the picks (Morozov et al., 1998). The plot in the bottom shows a ray diagram corresponding to two of the stronger reflectors in the above gathers. Horizontal scaling is the profile distance of Fig. 6.

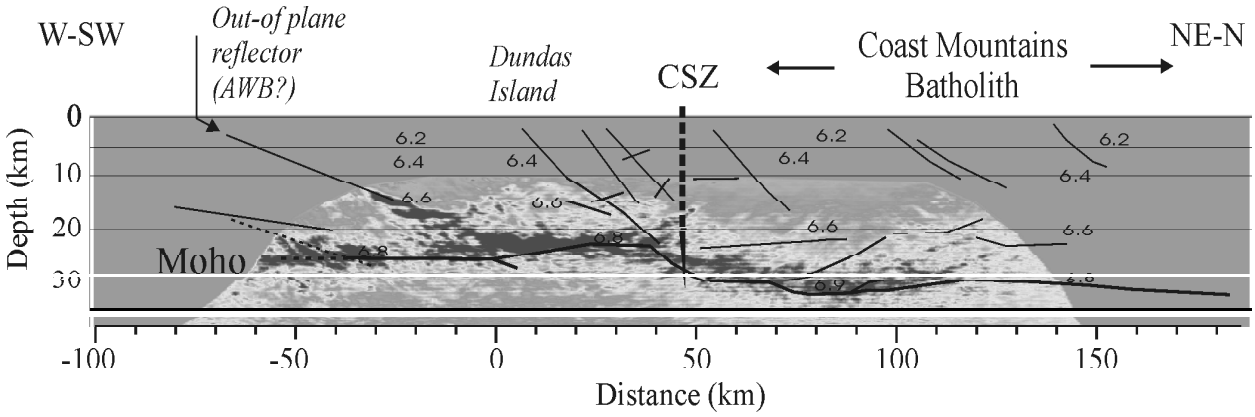

Fig. 8. Kirchhoff pre-stack migrated image of ACCRETE *PmP* reflections using the scheme described by Chen (1998). Trace envelope is used in order to reduce mis-stacking due to residual static problems. Note the continuous coverage of the Moho. The apparently NE dipping reflector in the SW part the model is interpreted as an out-of plane reflection from the Alexander-Wrangellia terrane boundary (see text for further discussion).

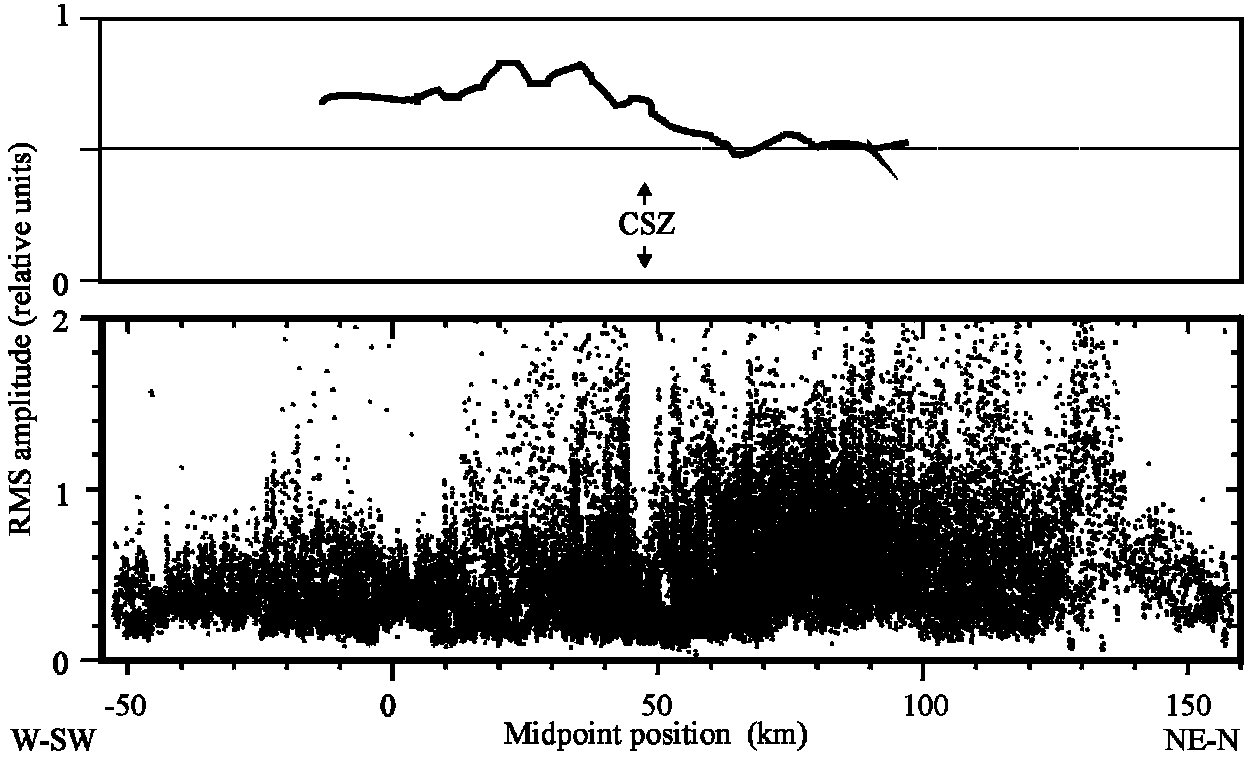

Fig. 9. *P*-wave Moho reflection amplitudes across the CSZ. *Top*: RMS amplitudes measured from the depth-migrated section (Fig. 8), within a 5-km window around Moho reflections. Note the increased reflection amplitudes west of the CSZ. *Bottom*: measured raw RMS amplitudes of Moho reflections plotted versus reflection midpoints. To compensate for geometric spreading, we applied a linear scaling with offset to the amplitudes. Note that the unmigrated amplitudes show no increase across the CSZ; instead, the Moho reflectivity appears to be higher under the CMB, east of the CSZ. Thus the increased migrated amplitudes west of the CSZ are due to better focusing of the image in this region (Fig. 8).

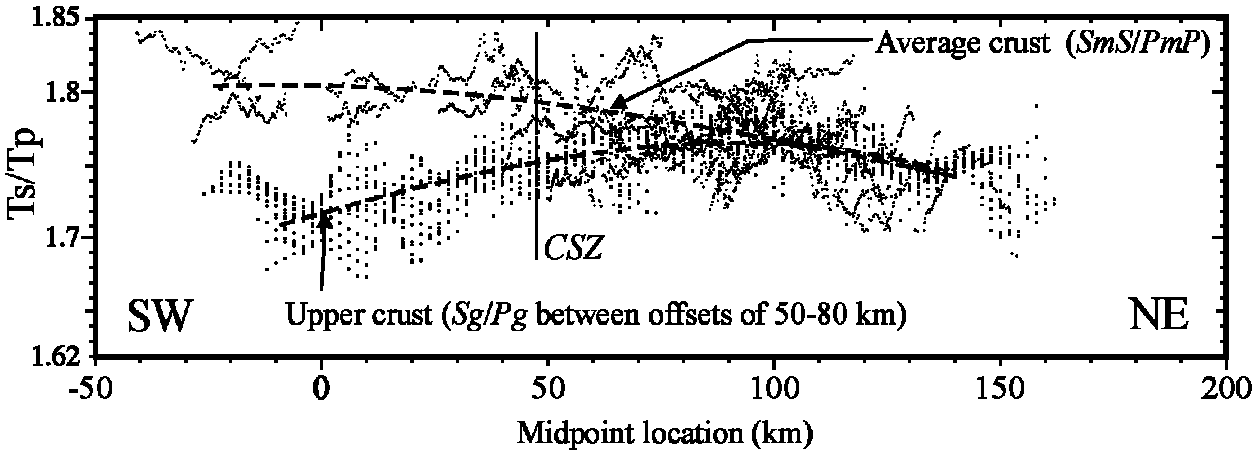

Fig. 10. Ratios of raw *S*-wave and *P*-wave travel times of the direct arrivals and of Moho reflections and their interpreted averages for the upper and entire crust (dashed lines). These ratios indicate a significant contrast in the *Vp*/*Vs* ratios between the upper and lower crust under the Insular superterrane (west of the CSZ) possibly related to oceanic lower crust. Compare this to the *Vp*/*Vs* model obtained by forward travel-time modeling (Fig. 11).

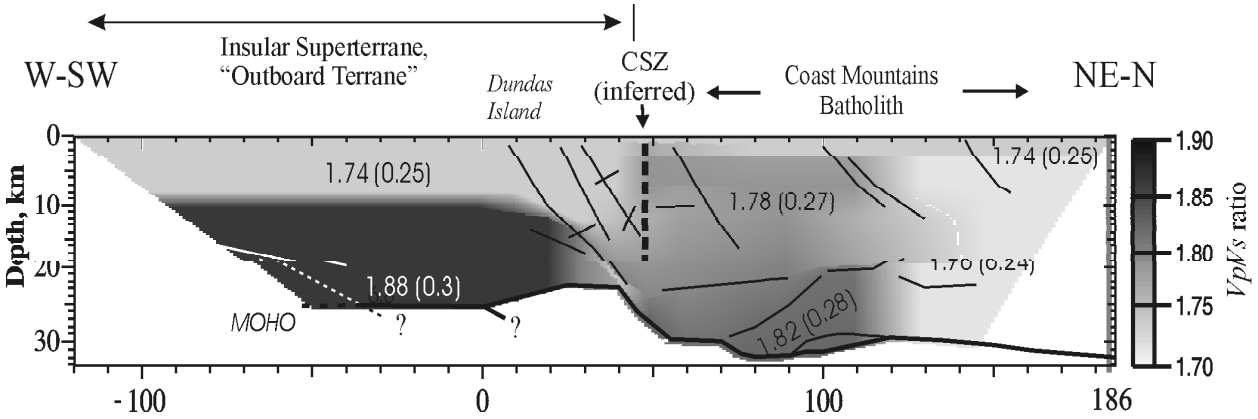

Fig. 11. *Vp*/*Vs* model obtained by joint travel-time inversion of all *P*- and *S*-wave arrivals and *P*/*S* conversions from the Moho. Note the contrast between three crustal blocks: the Alexander terrane, CMB (west of km 120) and the part of CMB approaching the Stikinia terrane east of km 120.

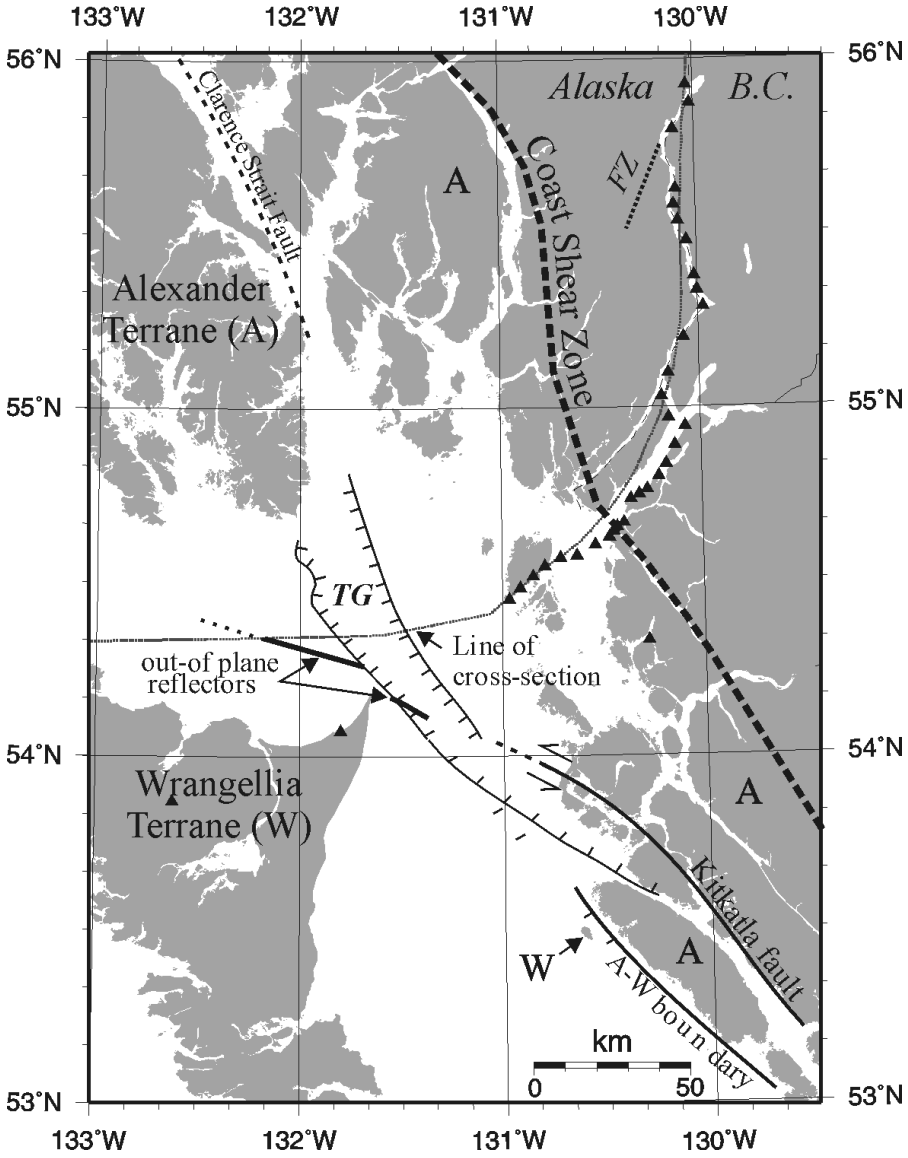

Fig. 12. Out-of plane, wide-angle reflections (heavy lines) that could be caused by an extension of Kitkatla fault or the Alexander-Wrangellia terrane boundary (AWB). An association of this reflector with the AWB is favored by the observed contrast in seismic properties between the Alexander and Wrangellia terranes (Figs. 6 and 11). This reflector is likely to be offset by the western flanks of Tertiary grabens (*TG*; Rohr and Currie, 1997). Fig. 13 shows an example of one of these reflections and of diffractions caused by such an offset of the boundary.

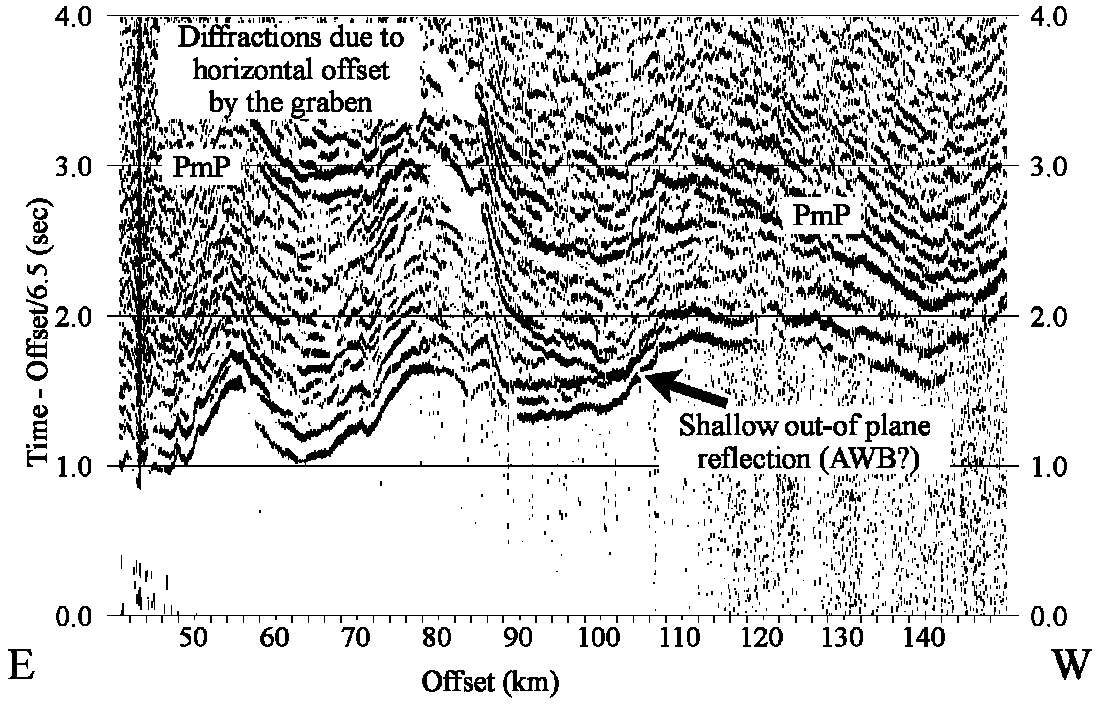

Fig. 13. Receiver gather from station 8 using airgun shots from the west (Fig. 1). The strong event (black arrow) merging with the first arrival near 110 km offset is interpreted as a reflection from the Alexander-Wrangellia terrane boundary (AWB, Fig.12) approaching the seismic line at an oblique angle. The termination of this reflection at a diffraction point (gray arrows) corresponds to the horizontal position of the western flank of a late Tertiary graben crossing the seismic line (*TG* in Fig. 12). Also note the expression of these grabens in up to 600 ms statics between the offsets of 50-90 km.